Rapid Communications

Theory of quantum oscillations in quasicrystals: Quantizing spiral Fermi surfaces

Stephen Spurrier and Nigel R. Cooper
T.C.M. Group, Cavendish Laboratory, University of Cambridge, JJ Thomson Avenue, Cambridge CB3 0HE, United Kingdom

(Received 9 November 2018; published 13 August 2019)

We show that electronic materials with disallowed rotational symmetries that enforce quasiperiodic order can exhibit quantum oscillations and that these are generically associated with exotic "spiral Fermi surfaces." These Fermi surfaces are self-intersecting, and characterized by a winding number of their surface tangent—a topological invariant—that is larger than one. We compute the nature of the quantum oscillations in two experimentally relevant settings which give rise to spiral Fermi surfaces: a "nearly-free-electron" quasicrystal, and 30° twisted bilayer graphene.

DOI: 10.1103/PhysRevB.100.081405

Introduction. Quasiperiodic systems are long-range ordered and yet nonperiodic [1,2]. This places them in a fascinating intermediate regime between periodic and disordered [3,4]. They first entered physics with the discovery by Shechtman *et al.* [5] of quasicrystals—electronic materials with crystallographically disallowed rotational symmetries [6]. However, due to the lack of Bloch's theorem, there still remain many open questions about their electronic properties. More recently, a surge of interest has risen due to the possibility of studying these questions in new, highly controllable, contexts such as cold atoms [7,8] and photonics [9], allowing for the exploration of physics such as localization [10–12], topology [13–19], and synthetic dimensions [8,20].

While progress is being made in artificial quasiperiodic systems, new avenues are also opening for electronic quasicrystals, including a recent realization of quasicrystalline 30° twisted bilayer graphene [21–23]. One of the key tools for studying periodic electronic materials are quantum oscillations [24–26]—a well-established technique for characterizing Fermi surfaces based on the semiclassical quantization of orbits into Landau levels [27,28]. For quasicrystals, one might expect that quantum oscillations are precluded by the lack of a well-defined Fermi surface or the typically low conductivity [4]. Nevertheless, an early experimental study surprisingly found these to be present [29]. Despite this finding, there has yet to be a theory developed to explain how quantum oscillations could occur in a quasicrystal [30,31].

In this Rapid Communication, we develop such a theory. We show how quantum oscillations can occur in quasicrystals, using two experimentally relevant models as examples: a nearly-free-electron quasicrystal [32–35,46] and 30° twisted bilayer graphene [21–23]. Surprisingly, we find that when quantum oscillations do occur, these are associated with a unconventional type of Fermi surface—which we dub a "spiral Fermi surface"—with topological character. Moreover, we find that the presence of a spiral Fermi surface in quasicrystals is generic—the only requirement is a separation in energy scales of their gaps [36,37].

The topology of the spiral Fermi surfaces is classified using the turning number N_t, which is defined as the winding number of the surface tangent—an invariant for two-dimensional plane curves [38,39]. A Fermi surface that can be smoothly deformed to a circle has $N_t = \pm 1$ and is considered trivial, while all other turning numbers are considered nontrivial. In quasicrystals, nontrivial turning numbers generically occur when the Fermi surface winds the pseudo-Brillouin-zone corner [36]. As such, the presence of nontrivial turning numbers is related to their crystallographically disallowed $2m$-fold rotational symmetry according to [36] (with quasicrystals satisfying $m \geqslant 4$)

$$N_t = \begin{cases} m-1 & \text{if } m \text{ even}, \\ (m-1)/2 & \text{if } m \text{ odd}. \end{cases} \tag{1}$$

Moreover, the turning number is measurable experimentally in quantum oscillations. This appears in the so-called Maslov contribution [28,40–43] to the offset γ in semiclassical quantization [24,26–28],

$$\ell_B^2 S(E) = 2\pi(n+\gamma), \tag{2}$$

where $\ell_B = \sqrt{\hbar/eB}$ is the magnetic length, $S(E)$ is the area swept out by the wave packet in reciprocal space, n is an integer, and

$$\gamma = \frac{N_t}{2} - \frac{\varphi_{\text{Berry}}}{2\pi}. \tag{3}$$

The first term of the right hand side is the topological Maslov contribution [28,40–43], while the second part is the geometrical Berry phase contribution [28,44].

Nearly-free-electron quasicrystal. Our first model is for a nearly-free-electron quasicrystal with an axis of tenfold rotational symmetry. This model is an approximation to icosahedral [5] and decagonal quasicrystals [45] that have nearly-free-electron qualities [35,46–50], such as the various aluminum-based quasicrystals studied in angle-resolved photoemission spectroscopy [32–34], and is known to exhibit a spiral holonomy [51]. We consider the two-dimensional single-particle spinless Hamiltonian $\hat{H} = \hat{\boldsymbol{p}}^2/2m + V(\hat{\boldsymbol{r}})$, with potential in real space given by [35,46,47]

$$V(\boldsymbol{r}) \equiv 2V_0 \sum_{j=1}^{5} \cos \boldsymbol{G}_j \cdot \boldsymbol{r}, \tag{4}$$

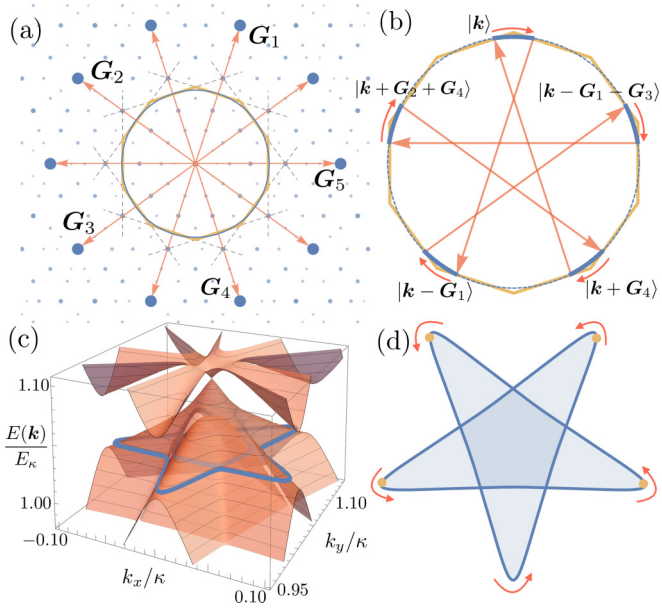

FIG. 1. Quantum oscillations in a nearly-free-electron quasicrystal. (a) Sketch of our model for a nearly-free-electron quasicrystal, consisting of ten Fourier components (largest blue points) at momenta $\pm\boldsymbol{G}_i$ (red arrows) which have Bragg planes (gray dotted lines) forming a pseudo-Brillouin zone (orange decagon) and which intersect the free-electron Fermi surface (blue circle). All combinations of these ten—the reciprocal lattice of periodic systems—cover k space densely (smaller blue points). (b) The semiclassical trajectories in an external magnetic field (solid blue curves) drift along the free-electron Fermi surface (dotted circle) with scattering by each $\boldsymbol{G}_i$ at the pseudo-Brillouin-zone boundary. (c) These semiclassical trajectories are seen as constant energy contours (blue curves) of an "effective band structure," which is shown for $V_0 = 0.1E_\kappa$. (d) The resulting spiral Fermi surface with nontrivial turning number of $N_t = 2$.

where $\boldsymbol{G}_j \equiv 2\kappa(\cos 2\pi j/5, \sin 2\pi j/5)$ and V_0 is the strength of each individual Fourier component, which is assumed to satisfy the nearly-free-electron limit $V_0 \ll E_\kappa \equiv \hbar^2\kappa^2/2m$. This model amounts to keeping the ten dominant Fourier components (i.e., the brightest spots in the diffraction pattern), in particular, those with Bragg planes that intersect the free-electron Fermi surface.

Our analysis of this model relies on the nearly-free-electron limit. This tells us that the free-electron Fermi surface [the blue circle shown in Fig. 1(a)] remains mostly unchanged except for the opening of gaps proportional to V_0 at intersections with Bragg planes to $\pm\boldsymbol{G}_i$ [dotted lines in Fig. 1(a)] and also gaps from combinations of n Bragg reflections. Since all combinations of $\boldsymbol{G}_i$ form a dense set in k space [shown in Fig. 1(a)], the set of all associated gaps will also be dense. Crucially, these gaps form a distinct hierarchy, $\Delta_{\text{gap}}^{n^{\text{th}}} \propto (V_0/E_\kappa)^n$. Thus, for V_0/E_κ small, one can choose a magnetic field that removes $(n+1)$th-order gaps via magnetic breakdown, while keeping nth-order gaps. The probability of magnetic breakdown is given by $P_{\text{MB}} = e^{-\pi ab\ell_B^2}$, where a and b are the axes of the avoided crossing hyperbola [43,52–55]. The simplest scenario is the regime of fields in which only first-order gaps are kept,

$$\left(\frac{V_0}{E_\kappa}\right)^4 \ll \frac{\hbar\omega_c}{E_\kappa} \ll \left(\frac{V_0}{E_\kappa}\right)^2, \tag{5}$$

where $\omega_c \equiv eB/m$ is the cyclotron frequency. We refer to this as the "first-order regime" of fields. The relevant gaps in this regime are along the pseudo-Brillouin-zone edges [yellow decagon in Fig. 1(b)].

Having specified an appropriate regime of magnetic fields—the first-order regime—the semiclassical trajectories can be found by tracing a path along the unperturbed free-electron Fermi surface and making jumps at intersections with relevant Bragg planes. This procedure is shown in Fig. 1(b) for a wave packet that is initially localized at the top of the pseudo-Brillouin zone in the free-particle state $|\boldsymbol{k}\rangle$. This state proceeds clockwise around the free-electron Fermi surface until it encounters the Bragg plane to $\boldsymbol{G}_1$, at which point it is scattered into the state $|\boldsymbol{k}-\boldsymbol{G}_1\rangle$. Continuing in this manner the wave packet is scattered a total of five times between the following states,

$$\begin{aligned}|\boldsymbol{k}\rangle \to |\boldsymbol{k}-\boldsymbol{G}_1\rangle \to |\boldsymbol{k}-\boldsymbol{G}_1-\boldsymbol{G}_3\rangle \\ \to |\boldsymbol{k}+\boldsymbol{G}_2+\boldsymbol{G}_4\rangle \to |\boldsymbol{k}+\boldsymbol{G}_4\rangle \to |\boldsymbol{k}\rangle,\end{aligned} \tag{6}$$

after which the wave packet returns and can be quantized according to (2).

By projecting onto the above subset of states we find an effective band structure, as shown in Fig. 1(c). The semiclassical trajectories described qualitatively above [blue curves in Fig. 1(b)] can now be seen quantitatively as the constant energy contours of this band structure shown in Figs. 1(c) and 1(d). The turning number can be computed by using a sum over the extremal points (points with vertical tangent), $N_t = \frac{1}{2}\sum_i \nu_i$, where $\nu_i = \pm 1$ for an extremal point with anticlockwise (clockwise) orientation. For the Fermi surface in Fig. 1(d), there are four extremal points (yellow dots) with anticlockwise orientation. This gives a turning number of $N_t = 2$, as expected from (1) with $m = 5$. This spiral Fermi surface (with $N_t = 2$) does not require fine tuning of the Fermi energy, unlike the "twisted Fermi surface" (with $N_t = 0$) of a tilted Weyl point [39].

We highlight two key signatures of this nontrivial turning number for quantum oscillations. The first is for the offset γ in the semiclassical quantization (2). A conventional Fermi surface that is deformable to a circle results in $\gamma = 1/2$, with deviations from this indicating a nonzero Berry phase. Here, $N_t = 2$ results in $\gamma = 0$ for *zero* Berry phase. The second signature is related to the "magnetic breakdown transition" as a function of magnetic field between first-order and second-order field regimes, shown in Fig. 2. As this transition occurs at a fixed Fermi energy, the total turning number is conserved [36]. Since the transition is between an odd number of dominant frequencies (a single frequency γ) and an even number (α and β), at least one Fermi surface must be nontrivial [36].

In order to address these results experimentally, one must consider three key parameters: the Fermi energy E_F, the field B, and the potential V_0. In typical nearly-free-electron quasicrystals, E_F is already at the required location—with the free-electron Fermi surface intersecting the pseudo-Brillouin-zone boundary [56]—therefore little to no doping should

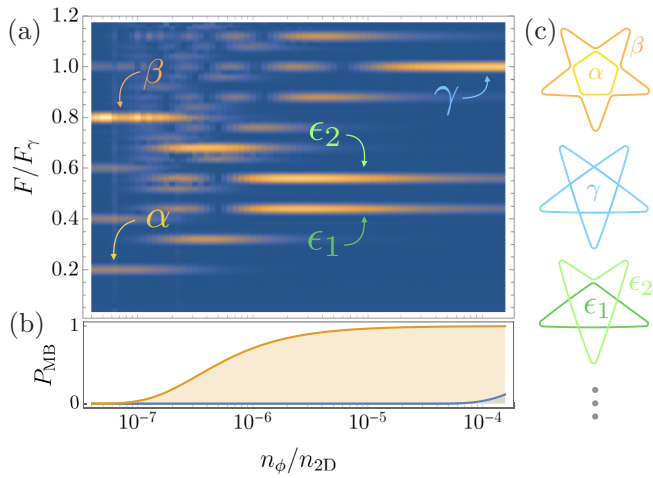

FIG. 2. Quantum oscillation frequency spectrum across the transition between second-order and first-order field regimes. (a) Density plot of the frequency spectrum (with frequencies given as a ratio of the spiral Fermi surface frequency F_γ) as a function of magnetic field (given in terms of $n_\phi = eB/h$ and $n_{2\mathrm{D}} = k_{\mathrm{F}}^2/2\pi$), for the parameters $V_0/E_\kappa = 0.01$ and $E_{\mathrm{F}}/E_\kappa = 1.01$. A transition is seen from a single frequency (γ) at high fields ($n_\phi/n_{2\mathrm{D}} \approx 10^{-4}$) to a pair of frequencies (α and β) at lower fields ($n_\phi/n_{2\mathrm{D}} \approx 10^{-7}$). (b) Plot of the magnetic breakdown probabilities at second-order gaps (orange curve) and first-order gaps (blue curve). (c) A selection of semiclassical contours used to label frequencies. For intermediate fields a complex mix of frequencies is present that can be labeled using intermediate contours such as ϵ_1 and ϵ_2.

be required. For the model parameters used in Fig. 2, the flux density required to reach the first-order regime is small compared to the electron density. Using typical experimental parameters of $\kappa = 1.3$ Å^{-1} and $m = m_{\mathrm{e}}$ (the free-electron mass) [33], this occurs for fields of $B \approx 10$ T—a regime attainable experimentally. The required potential V_0, however, provides the most severe constraint experimentally. The calculation of the magnetic breakdown transition in Fig. 2 allows us to quantify the maximum allowed V_0/E_κ—for a ratio that is too large the two regimes (first and second order) are not distinguishable. Using these criteria we find a maximum of $V_0/E_\kappa \approx 0.02$, which corresponds to a gap at the pseudo-Brillouin-zone edge of approximately 0.2 eV. Additionally, a small ratio of V_0/E_κ ensures the pseudogap at E_{F} is not fully formed [35], and the system remains metallic.

Twisted bilayer graphene. Our second model is for 30° twisted bilayer graphene, a system that has recently seen its first experimental realization [21–23]. This incommensurate superstructure satisfies the typical definition of a quasicrystal [1] in that its diffraction pattern contains sharp peaks possessing a $2m$-fold symmetry (here $m = 6$) that requires more basis vectors (four) than dimensions (two) in order to be indexed [57]. The quasiperiodic structure of the diffraction peaks is sufficient to cause the effective band structure to exhibit a spiral Fermi surface with a highly nontrivial turning number of $N_{\mathrm{t}} = 5$.

To show this, we use the model of twisted bilayer graphene developed in Ref. [58]. This takes a standard nearest-neighbor tight-binding Hamiltonian $H_\parallel$ for each layer, which is off diagonal in a Bloch basis $|\boldsymbol{k}, X\rangle$, with $X = A, B$ sublattice indices [59],

$$\langle \boldsymbol{k}, A|H_\parallel|\boldsymbol{k}, B\rangle = -t\sum_{i=1}^{3} e^{-i\boldsymbol{k}\cdot\boldsymbol{\rho}_i}, \tag{7}$$

where the vectors $\boldsymbol{\rho}_i$ connecting nearest neighbors in layer 1 are rotated by 30° with respect to those in layer 2. Tunneling between the layers causes a Bloch state from layer 1 with crystal momentum $\boldsymbol{k}$ to be coupled to all those from layer 2 with crystal momentum $\tilde{\boldsymbol{k}} = \boldsymbol{k} + \boldsymbol{G} - \tilde{\boldsymbol{G}}$ [58],

$$\langle \tilde{\boldsymbol{k}}, \tilde{X}|H_\perp|\boldsymbol{k}, X\rangle = -t_\perp(\boldsymbol{k} + \boldsymbol{G})e^{-i\boldsymbol{G}\cdot\boldsymbol{\tau}_X + i\tilde{\boldsymbol{G}}\cdot\boldsymbol{\tau}_{\tilde{X}}}, \tag{8}$$

where a tilde (no tilde) denotes layer 2 (1), $\boldsymbol{G}$ is a reciprocal lattice vector, $\boldsymbol{\tau}_X$ are position vectors of the sublattice sites within the unit cell, and $t_\perp(\boldsymbol{k})$ is radially symmetric and decays exponentially for $\boldsymbol{k}$ beyond the first Brillouin zone [60].

We analyze this model by assuming a weak coupling between the two layers, $t_\perp(\boldsymbol{k}) \ll t$. As with the nearly-free-electron limit in the previous section, this assumption is key to deriving meaningful semiclassical trajectories. In particular, this allows us to assert that the Fermi surfaces of each layer will be little affected, except at degenerate points that satisfy

$$E(\boldsymbol{k}) = \tilde{E}(\tilde{\boldsymbol{k}}), \quad \boldsymbol{k} + \boldsymbol{G} = \tilde{\boldsymbol{k}} + \tilde{\boldsymbol{G}}, \tag{9}$$

where $E(\boldsymbol{k})$ and $\tilde{E}(\tilde{\boldsymbol{k}})$ are the band structures of the unperturbed layers 1 and 2. This is considered a first-order coupling, as a gap will open proportional to $t_\perp$. However, there will also be gaps opened due to second-order processes that couple a layer to itself at the following degeneracies,

$$E(\boldsymbol{k}) = E(\boldsymbol{k} + \tilde{\boldsymbol{G}}), \quad \tilde{E}(\boldsymbol{k}) = \tilde{E}(\boldsymbol{k} + \boldsymbol{G}), \tag{10}$$

with these gaps proportional to $t_\perp^2/t$. For simplicity we choose to work in a field regime in which second-order, intralayer gaps can be ignored, while interlayer are kept—which can be safely assumed to exist given the weak-coupling assumption. However, this still leaves a dense set of gaps given by (9). Fortunately, many of these are exponentially small due to the $\boldsymbol{k}$ dependence of $t_\perp(\boldsymbol{k})$, as shown in Fig. 3(b). We therefore choose a field such that those gaps opened by the exponential tail of $t_\perp(\boldsymbol{k})$ beyond the first Brillouin zone are ignored. In this regime, one finds that spiral Fermi surfaces appear at those dopings for which the original Fermi surfaces of the two layers intersect.

Having determined a suitable field regime and doping, we derive the semiclassical trajectories by simply tracing a path along the unperturbed Fermi surfaces and switching between layers at the relevant intersections. If one begins this process, as shown in Fig. 3(c), on layer 1 (blue contour), the wave packet will progress anticlockwise before jumping to layer 2 (red contour). Here, it essentially repeats this contour again, now rotated by $5\pi/6$. This occurs a total of 12 times, resulting in a trajectory that winds the center a total of five times, as shown in Fig. 3(c). This is reflected in the effective Fermi surface shown in Fig. 3(d), shown for typical model parameters. The turning number is computed by summing over the extremal points (as discussed in the previous section). For each 2π winding about the center there are two extremal

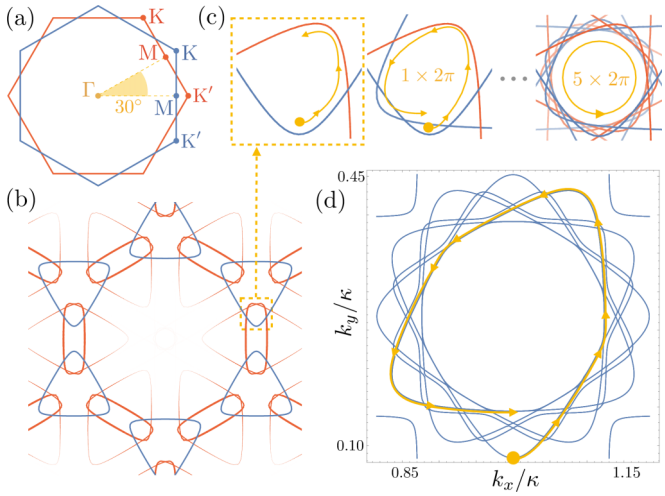

FIG. 3. Quantum oscillations in incommensurate 30° twisted bilayer graphene. (a) Sketch of each layer's Brillouin zone: Blue is referred to as layer 1 and red as layer 2. (b) The Fermi surface of layer 1 is coupled to the Fermi surface of layer 2, in addition to all possible translations of this Fermi surface by reciprocal lattice vectors from layer 1. (c) For sufficiently large doping, the Fermi surface of layer 1 intersects that of layer 2, allowing a semiclassical trajectory that jumps from layer 1 to layer 2. This repeats a total of 12 times before returning to be quantized by semiclassical quantization. (d) The Fermi surface of an effective model, shown for the experimental parameters given in Ref. [61].

points with anticlockwise orientation. As the Fermi surface winds the center five times, there are a total of ten extremal points with anticlockwise orientation, which means $N_t = 5$, as expected from (1) with $m = 6$.

Since the turning number in this case is odd, the two signatures highlighted in the previous section for a nearly-free-electron quasicrystal do not apply here—$\gamma = 1/2$, which is indistinguishable from the trivial case and breakdown transitions cannot identify odd turning numbers [36]. Instead, the key signature here is in the dependence of the quantum oscillation frequency on doping, as shown in Fig. 4. Below a critical doping of approximately 2 eV, the Fermi surfaces of each layer do not cross and only a single frequency is present, associated with a broadening Dirac cone. However, above 2 eV, the two layers' Fermi surfaces intersect and form three distinct contours: a square holelike contour that is topologically trivial ($N_t = -1$), a hexagonal electronlike contour that is also trivial ($N_t = 1$), and finally the nontrivial

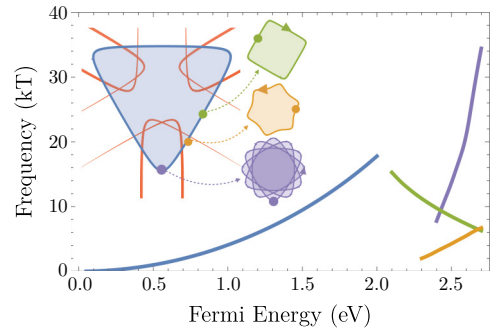

FIG. 4. Phenomenology for 30° twisted bilayer graphene. Plot of quantum oscillation frequencies as a function of doping away from charge neutrality, using the same parameters given in Fig. 3. Inset: Each frequency is identified with a different starting point on the unperturbed "Dirac" Fermi surface. The purple contours are those with a nontrivial turning number and have a larger than naively expected frequency.

($N_t = 5$) electronlike contour derived above. Crucially, the spiral Fermi surface is distinguished by a sharp increase of frequency with doping due to multiple overlapping Fermi surface areas.

We address the experimental feasibility by using tight-binding parameters for bilayer graphene [61]. This leaves two key parameters: the required field strength B and doping E_F. By extracting gap parameters we determine the required field to be $B \approx 7$ T, which is within experimental capabilities. The key challenge experimentally will be to reach a doping of $E_F \approx 2$ eV, although larger dopings have been realized experimentally for single layers [62].

In summary, we have used two very different models to show that quantum oscillations can arise in quasicrystalline materials. In both cases these are associated with spiral Fermi surfaces. In fact, this is a generic result, relying only on their unconventional rotational symmetry. As detailed in the Supplemental Material [36], this alone can be used to deduce the nontrivial turning number of the spiral Fermi surface. Moreover, that this arises for twisted bilayer graphene offers exciting opportunities for experimental observation.

In compliance with EPSRC policy framework on research data, all data are directly available within the publication.

Acknowledgments. We gratefully acknowledge support from EPSRC via Grants No. EP/K030094/1, No. EP/P034616/1, and No. EP/P009565/1, and from a Simons Investigator Award of the Simons Foundation.

[1] P. J. Steinhardt and S. Ostlund, *The Physics of Quasicrystals* (World Scientific, Singapore, 1987).
[2] H.-R. Trebin, *Quasicrystals: Structure and Physical Properties* (Wiley, Hoboken, NJ, 2006).
[3] J. Sokoloff, Phys. Rep. **126**, 189 (1985).
[4] S. Poon, Adv. Phys. **41**, 303 (1992).
[5] D. Shechtman, I. Blech, D. Gratias, and J. W. Cahn, Phys. Rev. Lett. **53**, 1951 (1984).
[6] D. Levine and P. J. Steinhardt, Phys. Rev. Lett. **53**, 2477 (1984).
[7] L. Guidoni, B. Dépret, A. di Stefano, and P. Verkerk, Phys. Rev. A **60**, R4233 (1999).
[8] K. Viebahn, M. Sbroscia, E. Carter, C. Yu, Jr., and U. Schneider, Phys. Rev. Lett. **122**, 110404 (2019).
[9] Y. S. Chan, C. T. Chan, and Z. Y. Liu, Phys. Rev. Lett. **80**, 956 (1998).
[10] L. Fallani, J. E. Lye, V. Guarrera, C. Fort, and M. Inguscio, Phys. Rev. Lett. **98**, 130404 (2007).

[11] M. Schreiber, S. S. Hodgman, P. Bordia, H. P. Lüschen, M. H. Fischer, R. Vosk, E. Altman, U. Schneider, and I. Bloch, Science **349**, 842 (2015).

[12] V. Khemani, D. N. Sheng, and D. A. Huse, Phys. Rev. Lett. **119**, 075702 (2017).

[13] Y. E. Kraus, Y. Lahini, Z. Ringel, M. Verbin, and O. Zilberberg, Phys. Rev. Lett. **109**, 106402 (2012).

[14] M. A. Bandres, M. C. Rechtsman, and M. Segev, Phys. Rev. X **6**, 011016 (2016).

[15] I. C. Fulga, D. I. Pikulin, and T. A. Loring, Phys. Rev. Lett. **116**, 257002 (2016).

[16] D.-T. Tran, A. Dauphin, N. Goldman, and P. Gaspard, Phys. Rev. B **91**, 085125 (2015).

[17] H. Huang and F. Liu, Phys. Rev. Lett. **121**, 126401 (2018).

[18] A. Dareau, E. Levy, M. B. Aguilera, R. Bouganne, E. Akkermans, F. Gerbier, and J. Beugnon, Phys. Rev. Lett. **119**, 215304 (2017).

[19] I. Dana, Phys. Rev. B **89**, 205111 (2014).

[20] Y. E. Kraus, Z. Ringel, and O. Zilberberg, Phys. Rev. Lett. **111**, 226401 (2013).

[21] S. J. Ahn, P. Moon, T.-H. Kim, H.-W. Kim, H.-C. Shin, E. H. Kim, H. W. Cha, S.-J. Kahng, P. Kim, M. Koshino, Y. W. Son, C.-W. Yang, and J. R. Ahn, Science **361**, 782 (2018).

[22] W. Yao, E. Wang, C. Bao, Y. Zhang, K. Zhang, K. Bao, C. K. Chan, C. Chen, J. Avila, M. C. Asensio, J. Zhu, and S. Zhou, Proc. Natl. Acad. Sci. USA **115**, 6928 (2018).

[23] Y.-R. Lin, N. Samiseresht, M. Franke, S. Parhizkar, S. Soubatch, B. Amorim, T.-L. Lee, C. Kumpf, F. Tautz, and F. C. Bocquet, arXiv:1809.07958.

[24] D. Shoenberg, *Magnetic Oscillations in Metals* (Cambridge University Press, Cambridge, UK, 2009).

[25] W. J. de Haas and P. M. van Alphen, Proc. R. Neth. Acad. Arts Sci. **33**, 170 (1930).

[26] I. Lifshitz and L. Kosevich, Sov. Phys. JETP **6**, 67 (1958).

[27] L. Onsager, Philos. Mag. **43**, 1006 (1952).

[28] D. Xiao, M.-C. Chang, and Q. Niu, Rev. Mod. Phys. **82**, 1959 (2010).

[29] E. Haanappel, Physica B **246-247**, 78 (1998).

[30] S. Roche and T. Fujiwara, Phys. Rev. B **58**, 11338 (1998).

[31] M. Krajcí and J. Hafner, J. Phys.: Condens. Matter **13**, 3817 (2001).

[32] E. Rotenberg, W. Theis, K. Horn, and P. Gille, Nature (London) **406**, 602 (2000).

[33] W. Theis, E. Rotenberg, K. J. Franke, P. Gille, and K. Horn, Phys. Rev. B **68**, 104205 (2003).

[34] V. A. Rogalev, O. Gröning, R. Widmer, J. H. Dil, F. Bisti, L. L. Lev, T. Schmitt, and V. N. Strocov, Nat. Commun. **6**, 8607 (2015).

[35] A. E. Carlsson, Phys. Rev. B **47**, 2515 (1993).

[36] See Supplemental Material at http://link.aps.org/supplemental/10.1103/PhysRevB.100.081405 for details on how our results in the main text are generalized, a derivation on how magnetic breakdown transitions at fixed Fermi energy can imply nontrivial turning numbers, details on how we calculate the magnetic breakdown transition spectrum, and for an argument on why perturbation theory is stable for our models, which contains Refs. [63–74].

[37] Throughout we use the word "gap" in reference to an avoided crossing between two energy levels—not in reference to a gap in the energy spectrum.

[38] H. Whitney, Compos. Math. **4**, 22 (1937).

[39] N. Bovenzi, M. Breitkreiz, T. E. O'Brien, J. Tworzydło, and C. W. J. Beenakker, New J. Phys. **20**, 023023 (2018).

[40] J. B. Keller, Ann. Phys. **4**, 180 (1958).

[41] V. I. Arnold, On a characteristic class arising in quantization conditions, in *Vladimir I. Arnold - Collected Works: Hydrodynamics, Bifurcation Theory, and Algebraic Geometry 1965-1972* (Springer, Berlin, 2014), pp. 85–97.

[42] A. M. Ozorio de Almeida, *Hamiltonian Systems: Chaos and Quantization* (Cambridge University Press, Cambridge, UK, 1990).

[43] A. Alexandradinata and L. Glazman, Phys. Rev. B **97**, 144422 (2018).

[44] G. P. Mikitik and Y. V. Sharlai, Phys. Rev. Lett. **82**, 2147 (1999).

[45] L. Bendersky, Phys. Rev. Lett. **55**, 1461 (1985).

[46] A. P. Smith and N. W. Ashcroft, Phys. Rev. Lett. **59**, 1365 (1987).

[47] J. P. Lu and J. L. Birman, Phys. Rev. B **36**, 4471 (1987).

[48] J. Friedel, Helv. Phys. Acta **61**, 538 (1988).

[49] V. Vaks, V. Kamyshenko, and G. Samolyuk, Phys. Lett. A **132**, 131 (1988).

[50] T. Fujiwara and T. Yokokawa, Phys. Rev. Lett. **66**, 333 (1991).

[51] S. Spurrier and N. R. Cooper, Phys. Rev. A **97**, 043603 (2018).

[52] M. H. Cohen and L. M. Falicov, Phys. Rev. Lett. **7**, 231 (1961).

[53] A. B. Pippard, Proc. R. Soc. London, Ser. A **270**, 1 (1962).

[54] E. I. Blount, Phys. Rev. **126**, 1636 (1962).

[55] J. R. Reitz, J. Phys. Chem. Solids **25**, 53 (1964).

[56] This well-known condition is closely connected to the stability of the quasicrystalline phase, often referred to as the Hume-Rothery rule [4,46,75–77].

[57] It does not satisfy other definitions of a quasicrystal [78].

[58] M. Koshino, New J. Phys. **17**, 015014 (2015).

[59] A. H. Castro Neto, F. Guinea, N. M. R. Peres, K. S. Novoselov, and A. K. Geim, Rev. Mod. Phys. **81**, 109 (2009).

[60] We use $t_\perp(\boldsymbol{k}) = (2/\sqrt{3}a^2)\int d^2r\, e^{-i\boldsymbol{k}\cdot\boldsymbol{r}} T_\perp(\boldsymbol{r} + d\boldsymbol{e}_z)$, where $T_\perp(\boldsymbol{R}) = -V^0_{pp\sigma} e^{(R-d)/r_0}$, a is the lattice constant, and d is the layer separation, from Ref. [58].

[61] We use the following parameters for bilayer graphene, $t = -2.7$ eV, $V^0_{pp\sigma} = 0.48$ eV, $a = 0.246$ nm, $d = 0.335$ nm, $r_0 = 0.184a$, and $\kappa = 2\pi/\sqrt{3}a$, from Ref. [58].

[62] J. L. McChesney, A. Bostwick, T. Ohta, T. Seyller, K. Horn, J. González, and E. Rotenberg, Phys. Rev. Lett. **104**, 136803 (2010).

[63] Y. Zhang, A. V. Maharaj, and S. Kivelson, Phys. Rev. B **91**, 085105 (2015).

[64] J. P. Lu and J. L. Birman, Phys. Rev. B **38**, 8067 (1988).

[65] S. Burkov, T. Timusk, and N. Ashcroft, J. Phys.: Condens. Matter **4**, 9447 (1992).

[66] J. M. Lee, *Riemannian Manifolds: An Introduction to Curvature*, Vol. 176 (Springer, Berlin, 2006).

[67] F. Fillastre and I. Izmestiev, arXiv:1702.02114.

[68] A. A. Slutskin, JETP Lett. **26**, 474 (1968).

[69] E. I. Dinaburg and Y. G. Sinai, Funct. Anal. Appl. **9**, 279 (1975).

[70] J. H. Lowenstein, *Essentials of Hamiltonian Dynamics* (Cambridge University Press, Cambridge, UK, 2012).

[71] Y. Bugeaud, *Distribution Modulo One and Diophantine Approximation* (Cambridge University Press, Cambridge, UK, 2012), Vol. 193.

[72] K. Suzuki and R. Okamoto, Prog. Theor. Phys. **70**, 439 (1983).

[73] Note that the phases we use differ from those of Refs. [43,68]. They are chosen here such that the theory produces the expected results in the two limits of $\rho \to 0,\ 1$.

[74] We process our data using an apodization, specifically, a Kaiser window with parameter $\alpha = 1.7$. This smoothly tapers the data to zero at the boundaries, suppressing unwanted "artifacts" that occur due to an otherwise sharp truncation.

[75] P. A. Bancel and P. A. Heiney, Phys. Rev. B **33**, 7917 (1986).

[76] J. Hafner and M. Krajčí, Phys. Rev. Lett. **68**, 2321 (1992).

[77] I. Martin, S. Gopalakrishnan, and E. A. Demler, Phys. Rev. B **93**, 235140 (2016).

[78] T. Yu and L. Liao, arXiv:1808.08730.